



Publication Year	2016
Acceptance in OA	2020-04-29T14:23:00Z
Title	On the Nature of Hydrostatic Equilibrium in Galaxy Clusters
Authors	BIFFI, Veronica, BORGANI, STEFANO, MURANTE, Giuseppe, RASIA, ELENA, Planelles, S., GRANATO, Gian Luigi, Ragone-Figueroa, C., Beck, A. M., GASPARI, MASSIMO, Dolag, K.
Publisher's version (DOI)	10.3847/0004-637X/827/2/112
Handle	http://hdl.handle.net/20.500.12386/24329
Journal	THE ASTROPHYSICAL JOURNAL
Volume	827



ON THE NATURE OF HYDROSTATIC EQUILIBRIUM IN GALAXY CLUSTERS

V. BIFFI^{1,2}, S. BORGANI^{1,2,3}, G. MURANTE², E. RASIA^{2,4}, S. PLANELLES^{1,2,5}, G. L. GRANATO², C. RAGONE-FIGUEROA⁶, A. M. BECK⁷,
M. GASPARI^{8,9}, AND K. DOLAG⁷

¹ Astronomy Unit, Department of Physics, University of Trieste, via Tiepolo 11, I-34131 Trieste, Italy; biffi@oats.inaf.it

² INAF, Osservatorio Astronomico di Trieste—OATs, via Tiepolo 11, I-34131 Trieste, Italy

³ INFN—National Institute for Nuclear Physics, Via Valerio 2, I-34127 Trieste, Italy

⁴ Department of Physics, University of Michigan, 450 Church Street, Ann Arbor, MI 48109, USA

⁵ Departamento de Astronomía y Astrofísica, Universidad de Valencia, c/Dr. Moliner, 50, E-46100—Burjassot (Valencia), Spain

⁶ Instituto de Astronomía Teórica y Experimental (IATE), Consejo Nacional de Investigaciones Científicas y Técnicas de la República Argentina (CONICET), Observatorio Astronómico, Universidad Nacional de Córdoba, Laprida 854, X5000BGR, Córdoba, Argentina

⁷ University Observatory Munich, Scheinerstr. 1, D-81679 Munich, Germany

⁸ Department of Astrophysical Sciences, Princeton University, Princeton, NJ 08544, USA

Received 2015 December 31; revised 2016 April 11; accepted 2016 June 16; published 2016 August 12

ABSTRACT

In this paper, we investigate the level of hydrostatic equilibrium (HE) in the intracluster medium of simulated galaxy clusters, extracted from state-of-the-art cosmological hydrodynamical simulations performed with the Smoothed-Particle-Hydrodynamic code GADGET-3. These simulations include several physical processes, among which are stellar and active galactic nucleus feedback, and have been performed with an improved version of the code that allows for a better description of hydrodynamical instabilities and gas mixing processes. Evaluating the radial balance between the gravitational and hydrodynamical forces via the gas accelerations generated, we effectively examine the level of HE in every object of the sample and its dependence on the radial distance from the center and on the classification of the cluster in terms of either cool-core or dynamical state. We find an average deviation of 10%–20% out to the virial radius, with no evident distinction between cool-core and non-cool-core clusters. Instead, we observe a clear separation between regular and disturbed systems, with a more significant deviation from HE for the disturbed objects. The investigation of the bias between the hydrostatic estimate and the total gravitating mass indicates that, on average, this traces the deviation from HE very well, even though individual cases show a more complex picture. Typically, in the radial ranges where mass bias and deviation from HE are substantially different, the gas is characterized by a significant amount of random motions ($\gtrsim 30\%$), relative to thermal ones. As a general result, the HE-deviation and mass bias, at a given distance from the cluster center, are not very sensitive to the temperature inhomogeneities in the gas.

Key words: galaxies: clusters: general – galaxies: clusters: intracluster medium – methods: numerical

1. INTRODUCTION

As fair samples of the universe, galaxy clusters are dominated in mass, $\sim 80\%$, by dark matter (DM) but also comprise a significant amount of baryonic visible matter, in the form of galaxies and hot plasma ($\sim 5\%$ and $\sim 15\%$ in mass, respectively). In the accepted scenario of hierarchical structure formation, clusters grow via smooth accretion processes as well as through merger events (see Kravtsov & Borgani 2012 for a review). According to this theoretical framework, the hot intracluster medium (ICM) is assumed to collapse within the cluster DM halo, to get shock heated during the assembly process, and to finally settle with temperatures of the order of 10^7 – 10^8 K, reflecting the depth of the potential well ($\sim 10^{14}$ – $10^{15} M_\odot$). The dynamics of the intracluster gas can be described by the Euler equation:

$$\frac{d\mathbf{v}}{dt} = -\nabla\Phi - \frac{1}{\rho}\nabla P. \quad (1)$$

Here, P is the total gas pressure, Φ is the cluster potential, and

$$\frac{d\mathbf{v}}{dt} = \frac{\partial\mathbf{v}}{\partial t} + (\mathbf{v} \cdot \nabla)\mathbf{v} \quad (2)$$

is the Lagrangian derivative of the velocity or the sum of the acceleration and the inertia terms, respectively, the first and

second term on the lhs of Equation (2). The condition of hydrostatic equilibrium (HE) is represented by

$$\frac{d\mathbf{v}}{dt} = 0. \quad (3)$$

This assumption implies that the net Lagrangian three-dimensional acceleration of the gas, resulting from the sum of hydrodynamical and gravitational forces, is null. With our numerical study, we intend to investigate whether the condition expressed by Equation (3), and so the balance between hydrodynamical and gravitational forces, is reliable in cosmological simulations of galaxy clusters, when evaluated at typical, interesting distances from the cluster center. In fact, the assumption of HE is the key ingredient behind one of the most diffuse methods employed to measure the mass of galaxy clusters (as well as large ellipticals; e.g. Pellegrini et al. 2006 and references therein), which is the crucial property necessary to characterize a cluster for astrophysical as well as cosmological purposes.

Specifically, the reconstruction of the so-called hydrostatic mass from X-ray observations of the ICM thermal properties can be derived from Equation (3), re-formulated as

$$0 = -\nabla\Phi - \frac{1}{\rho}\nabla P,$$

⁹ Einstein and Spitzer Fellow.

along with the additional assumptions of spherical symmetry and of a purely thermal pressure support of the gas ($P = P_{\text{th}}$). Under these conditions, and further assuming the equation of state of an ideal gas to hold for the ICM, one can derive the total mass from the profiles of gas density (ρ) and temperature (T):

$$M_{\text{HE}}(<r) = -\frac{k_B T(r)r}{\mu G m_p} \left[\frac{d \log \rho(r)}{d \log r} + \frac{d \log T(r)}{d \log r} \right], \quad (4)$$

where k_B is the Boltzmann constant, μ is the mean molecular weight, G is the gravitational constant, and m_p is the proton mass.

For regular virialized galaxy clusters, the above assumptions are a reasonable representation of the gas state. However, if any of the hypotheses done are not satisfied, the hydrostatic mass might provide a biased estimate of the true gravitating mass.

Observationally, the particular composition of galaxy clusters allows us to observe them in many different wavelengths other than X-rays, such as optical or millimetric bands, providing independent methods to reconstruct their intrinsic structure and total mass (see, e.g., Mahdavi et al. 2008, 2013; von der Linden et al. 2014; Applegate et al. 2015; Sereno & Etori 2015; Simet et al. 2015; Smith et al. 2016). Some of these approaches, such as the one based on optical observations of the weak lensing effect, are less sensitive to the complex non-gravitational processes that characterize the gas and have been commonly used for comparisons to X-ray mass estimates (e.g., Donahue et al. 2014). A mismatch between optical and X-ray mass measurements has been often interpreted as a lack of HE. Nonetheless, the observational estimate of the the X-ray temperature may also cause an additional bias because of the uncertainties on the calibration of the X-ray instrument used to estimate the hydrostatic mass (see, e.g., the differences between Chandra and XMM, as reported by Nevalainen et al. 2010; Schellenberger et al. 2015). Furthermore, it is important to notice that the violation of *any* of the assumptions behind Equation (4) can lead to a bias in the mass estimate, even in the presence of a perfect balance between gravity and pressure.

To this end, numerical studies based on state-of-the-art cosmological hydrodynamical simulations of galaxy clusters offer an optimal way of tackling the problem. Several groups have explored the hydrodynamical stability of simulated clusters, computing the thermal and non-thermal components derived from Equations (1) and (2) that contribute to the total support against the cluster gravitational potential and, if neglected, induce the hydrostatic mass bias. In fact, hydrodynamical simulations show that a non-negligible fraction of the ICM pressure support is due to turbulent and bulk gas motions, and this should be taken into account for the mass estimation based on HE (Rasia et al. 2004; Fang et al. 2009; Lau et al. 2009, 2013; Vazza et al. 2009; Biffi et al. 2011; Gaspari & Churazov 2013; Suto et al. 2013; Gaspari et al. 2014; Nelson et al. 2014). However, previous attempts to specifically identify the principal sources of bias led to different conclusions, mainly because of differences in the terminology, computational method, or interpretation of the mass terms involved (Lau et al. 2013; Suto et al. 2013; Shi et al. 2015). In Fang et al. (2009), the major source of additional pressure support against gravity has been ascribed to gas rotational patterns, especially in the center of relaxed

systems, while, in Lau et al. (2009), the authors found a significantly higher contribution to the total pressure support coming from random motions. More recently, numerical investigations by Suto et al. (2013) and Nelson et al. (2014) additionally explored the possibility of a non-steady state of the gas, i.e., $\partial v / \partial t \neq 0$, in Equation (2), and assessed the importance of accounting for gas acceleration as well. The common finding of numerical works is that, even for very regular clusters, the hydrostatic mass overall underestimates the true gravitating mass by a typical factor of 10%–20% (see, e.g., Rasia et al. 2004, 2006; Jeltema et al. 2008; Piffaretti & Valdarnini 2008; Meneghetti et al. 2010; Nelson et al. 2012). Independently of this, the presence of gas temperature inhomogeneities can cause an additional bias in the temperature estimate from current X-ray telescopes, thus originating a total difference between X-ray derived and true masses of up to 30% (e.g., Rasia et al. 2014).

Even if challenging, the detection of gas turbulent and bulk motions will substantially improve with observations from next-generation X-ray calorimeters, on board satellites such as ASTRO-H¹⁰ or Athena.¹¹ Their unprecedented level of energy resolution will eventually allow us to put tighter constraints on the ICM motions, measuring gas velocities from the broadening and center shifts of heavy ions emission lines in the X-ray spectra down to a few hundred km s^{-1} (Biffi et al. 2013; Etori et al. 2013; Nandra et al. 2013).

Nonetheless, it is very difficult to measure corrections for the mass bias and general deviations from HE of the gas on a single cluster base at intermediate-high redshift where the spatial precision is more limited, and therefore a statistical approach is preferable. In fact, a thorough investigation of the origin of HE violation for individual cases can only be pursued via numerical simulations, which grant access to the full three-dimensional thermal and velocity structure of clusters and to their dynamical history. Complementary to this, simulations can also be exploited to provide general predictions for cluster populations selected on the base of common thermal or dynamical properties, more similarly to the observational approach. Even though gas motions might be constrained in the future, it remains extremely challenging to observationally distinguish the intrinsic deviation from the assumption of the steady state and other sources of mass bias (e.g., sphericity and non-thermal pressure). Certainly, the general relation between the common definition of hydrostatic mass bias and the deviation from HE by means of numerical studies is worth further investigation.

Here, instead of focusing on the various terms from which the mass bias originate, we take a step back with respect to the previous numerical studies and explore, from a more elementary perspective, the primary assumption of the HE expressed by Equation (3) and intended as a balance of gravitational and hydrodynamical forces. Despite the fact that the mass bias is the observable quantity, our numerical approach represents a unique opportunity to quantify the intrinsic deviation from HE, and consequently its connection to the mass bias, its dependence on the cluster thermodynamical properties, and its relation to the level of random and bulk motions in the gas. Specifically, we propose the investigation of the level of HE of the ICM in simulated clusters, expressed

¹⁰ <http://astro-h.isas.jaxa.jp/en/>

¹¹ <http://www.the-athena-x-ray-observatory.eu/>

by condition (3), by exploring the three-dimensional gas acceleration field.

The use of state-of-the-art cosmological hydrodynamical simulations of galaxy clusters allows us to directly evaluate (1) the balance between hydrodynamical and gravitational forces through the comparison of the accelerations derived from the two terms, (2) the dependence on the distance from the cluster center, and (3) the possible connections to the thermodynamical state of the system.

This paper is organized as follows. We present the simulations of galaxy clusters used for the present study in Section 2, while in Section 3 describe the method to evaluate the level of HE in the simulated clusters and clarify the terminology used. Our results are presented in Section 4, where we discuss the relation between the level of HE and the cluster dynamical and thermal structure, as well as its relation to mass and temperature bias. Finally, we draw our conclusions in Section 5.

2. THE SIMULATED DATA SET

The data set used in this work is composed of a sample of 29 simulated clusters analyzed at $z = 0$. Among them, 24 are massive systems with $M_{200} > 8 \times 10^{14} h^{-1} M_{\odot}$ and 5 are smaller objects with M_{200} in the range of $1-4 \times 10^{14} h^{-1} M_{\odot}$ (Planelles et al. 2014). These clusters have been selected as the most massive halos residing at the center of 29 Lagrangian regions, resimulated from zoomed initial conditions (the same as those in Bonafede et al. 2011), with the Tree-PM Smoothed-particle-hydrodynamics (SPH) code GADGET-3 (Springel 2005). The simulations assume a Λ CDM cosmological model with $\Omega_m = 0.24$, $\Omega_b = 0.04$, $H_0 = 72 \text{ km s}^{-1} \text{ Mpc}^{-1}$, $n_s = 0.96$, and $\sigma_8 = 0.8$. The mass resolution of this set is $m_{\text{DM}} = 8.47 \times 10^8 M_{\odot}$ for the DM particles, and $m_{\text{gas}} = 1.53 \times 10^8 M_{\odot}$ for the initial gas particle mass. The Plummer-equivalent softening length for the computation of the gravitational force is $\epsilon = 3.75 h^{-1} \text{ kpc}$ for DM and gas particles, $\epsilon = 2 h^{-1} \text{ kpc}$ for star and black hole particles at $z = 0$.

The version of the code used here includes the improved version of the hydrodynamical scheme described in Beck et al. (2016), which largely improves the SPH capability to follow gas-dynamical instabilities and mixing processes, and prevents particle clumping. In particular, these new developments include a higher-order interpolation kernel as well as time-dependent formulations for artificial viscosity and artificial thermal diffusion. More details on the hydrodynamical method as well as a large set of standard tests are presented in Beck et al. (2016).

The physical processes treated in the simulations comprise metallicity-dependent radiative cooling, time-dependent UV background, star formation from a multi-phase interstellar medium (Springel & Hernquist 2003), metal enrichment from supernovae (SN) II, SN Ia, and asymptotic-giant-branch stars (Tornatore et al. 2004, 2007), SN-driven kinetic feedback in the form of galactic winds (with 350 km s^{-1} velocity), and the novel model for active galactic nucleus thermal feedback, presented in Steinborn et al. (2015), in which cold and hot gas accretion onto black holes (BHs) is treated separately. In particular, we consider here only the cold-phase accretion, assuming $\alpha_{\text{cold}} = 100$ as a boost factor of the Bondi rate for the Eddington-limited gas accretion onto the BH (see also Gaspari et al. 2015).

For this paper, we employ a set of simulations in which all of the above physical processes are included. This allows us to reproduce the ICM as realistically as possible. This new set of simulations has recently been presented in Rasia et al. (2015), where it was shown for the first time how it was possible to recover the observed coexistence of cool-core (CC) and non-cool-core (NCC) clusters (Rasia et al. 2015). More results on the simulations will also be presented in forthcoming papers (G. Murante et al. 2016, in preparation; S. Planelles et al. 2016, in preparation).

3. CHARACTERIZING THE DEVIATION FROM HE

With the use of hydrodynamical simulations, it is possible to directly trace the 3D structure of the gas acceleration field. In particular, from the GADGET code, we obtain the value of the gas total acceleration (dv/dt , Equation (2)) for each gas particle in the simulation output, explicitly separated in its gravitational and hydrodynamical components.

In order to satisfy the hydrostatic equilibrium, the two acceleration components must balance:

$$\text{HE:} \quad 0 = \frac{dv}{dt} = \mathbf{a} = \mathbf{a}_g + \mathbf{a}_h. \quad (5)$$

In general, the equilibrium in Equation (5) should be evaluated separately for each component of the acceleration vector. However, in the case of astronomical objects such as galaxy clusters or stars, the condition has to hold radially. For this reason, we consider only the radial component of the accelerations \mathbf{a}_g and \mathbf{a}_h , indicated as \mathcal{G}_r and \mathcal{H}_r , respectively, that we averaged within spherical shells.

3.1. Method

We investigate deviations from HE by studying the deviation from -1 of the ratio, $\mathcal{G}_r/\mathcal{H}_r$, between the radial components of gravitational and hydrodynamical accelerations.

To compute radial profiles of the $\mathcal{G}_r/\mathcal{H}_r$ term, two alternative approaches have been used:

- i. evaluating the $\mathcal{G}_r/\mathcal{H}_r$ ratio particle-by-particle and then averaging over the spherical shell;
- ii. building the profiles of the two accelerations separately and then computing the ratio of the \mathcal{G}_r radial profile to the \mathcal{H}_r radial profile.

Methods (i) and (ii) are equivalent in the ideal case of a spherical gas distribution in HE and without inhomogeneities (see the Appendix).

We note that all the calculations have been done by subtracting a bulk gravitational acceleration, which in principle can be non-negligible. This is calculated as a mass-weighted mean value within R_{200} , considering all the particle species (i.e., DM, gas, and stars). The mean value of the hydrodynamical component is not accounted for because it is typically very low. We verified that for all the 29 main halos in the sample, both acceleration components are indeed very low.

The gas particles used for the calculation are those in the hot phase. Namely, we remove from the computation the cold gas ($T < 3 \times 10^4 \text{ K}$), and the multi-phase gas particles, which have a cold mass fraction greater than 10%.

Given the purposes of our investigation, we do not remove any substructure.

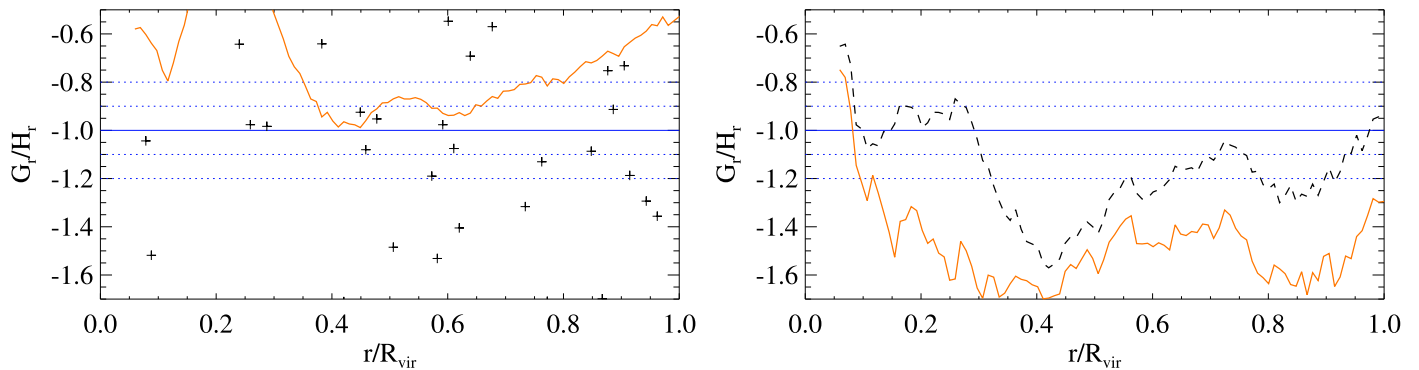


Figure 1. Radial profiles of the $\mathcal{G}_r/\mathcal{H}_r$ ratio for one simulated cluster (D8) of the sample. Left: mean (black crosses) and median (orange, solid line) profiles calculated from the particle-by-particle values of $\mathcal{G}_r/\mathcal{H}_r$; right: mean (black, dashed line) and median (orange, solid line) $\mathcal{G}_r/\mathcal{H}_r$ profiles calculated from the radial profiles of the two separate components \mathcal{G}_r and \mathcal{H}_r .

3.2. Terminology

We summarize here the meaning of the quantities and assumptions employed.

- Acceleration term: this is the total derivative dv/dt in Equation (1), which contains both the pure acceleration term $\partial v/\partial t$ and the inertia term $(v \cdot \nabla)v$; as previously explained, we will refer to this term in the form of $\mathcal{G}_r/\mathcal{H}_r$, assuming spherical symmetry and considering the radial component of the acceleration only.
- HE: from Equation (5), HE is quantified by $\mathcal{G}_r/\mathcal{H}_r = -1$, with the underlying assumption of spherical symmetry;
- Deviation from HE:

$$\delta_{\text{HE}} = \mathcal{G}_r/\mathcal{H}_r + 1;$$

- M_{HE} : this indicates the hydrostatic mass and implies the assumptions of HE, spherical symmetry, and the purely thermal nature of the pressure.
- Hydrostatic-mass bias:

$$b_M = (M_{\text{HE}} - M_{\text{true}})/M_{\text{true}},$$

where M_{true} is the total gravitating mass of the system, computed summing up all the particle masses (within the considered radius).

It is important to notice that (b) and (d) are derived from the left- and right-hand side terms of Equation (1) but do not share the same assumptions, as purely thermal pressure is assumed only when M_{HE} is calculated.

4. RESULTS

4.1. Application to Simulated Galaxy Clusters

By applying the method described in the previous section to simulated galaxy clusters, we can gain a deeper understanding of the intrinsic state of the ICM, in the presence of several astrophysical phenomena, such as star formation, feedback processes, and accretion of substructures. Moreover, we can explore the validity of the HE assumption and its influence on the median behavior in different populations of clusters.

For the purpose of showing how complex the level of HE deviation is at different radii, we start by considering one single object, shown in Figure 1.

We notice the evident difference between the methods (i) and (ii) described in Section 3. In particular, both the mean (black, dashed curve) and median profiles (orange, solid curve)

are smoother when we measure the ratio of the two profiles (see right panel in Figure 1).

The different picture drawn from the particle-based approach (left panel in Figure 1) can be ascribed to the inhomogeneous distribution of the gas accelerations and to the large spread of the hydrodynamical acceleration values, which is considerably broader than the gravitational one. Furthermore, the kernels used to smooth the hydrodynamical and gravitational forces are different. Therefore, the accelerations are evaluated at two unequal scales. Furthermore, numerical terms (e.g., artificial viscosity and diffusion) intervene in the SPH implementation of the Euler equation, so that Equation (1) is not satisfied in its theoretical formulation on a particle base. In the following, we use the second approach where we compute the two \mathcal{G}_r and \mathcal{H}_r components separately and subsequently we calculate the ratio $\mathcal{G}_r/\mathcal{H}_r$ from their profiles.

The cluster shown in Figure 1 represents a rather extreme case, with deviations up to $\sim 50\%$ or more, already outside the inner region ($>0.1 R_{\text{vir}}$), indicating a non-negligible violation of the HE assumption and possible biases in the HE-derived mass estimate.

In general, among the 29 clusters of the sample, the individual profiles show significant variations and a close inspection to the distribution of each cluster substructures, merging and thermal history would be necessary to understand the detailed features of the $\mathcal{G}_r/\mathcal{H}_r$ profiles.

4.2. On the Relation to the Hydrostatic Mass Bias

For each cluster in the sample, we calculate the hydrostatic mass as in Equation (4). For the purpose of our theoretical investigation, we do not apply any substructure removal from the ICM. In principle, the hydrostatic mass bias, b_M (definition (e), in Section 3), does quantify the deviation from HE as long as the additional hypotheses on which the hydrostatic mass relies are valid. Therefore, it is interesting to compare the radial profiles of $\mathcal{G}_r/\mathcal{H}_r$ and mass bias.

In order to explore the origin of the differences between mass bias and deviation from HE, it is also useful to investigate possible connections to the level of non-thermal motions of the gas, which are typically not accounted for in the usual hydrostatic mass estimate.

In Figure 2, we present, for three clusters of the sample, the separate profiles of the two accelerations (left panels), the direct comparison of mass bias and deviation from HE (central panels), and the ratio $\sigma_r^2/\sigma_{\text{therm,1D}}^2$ (right panels), where σ_r^2 is

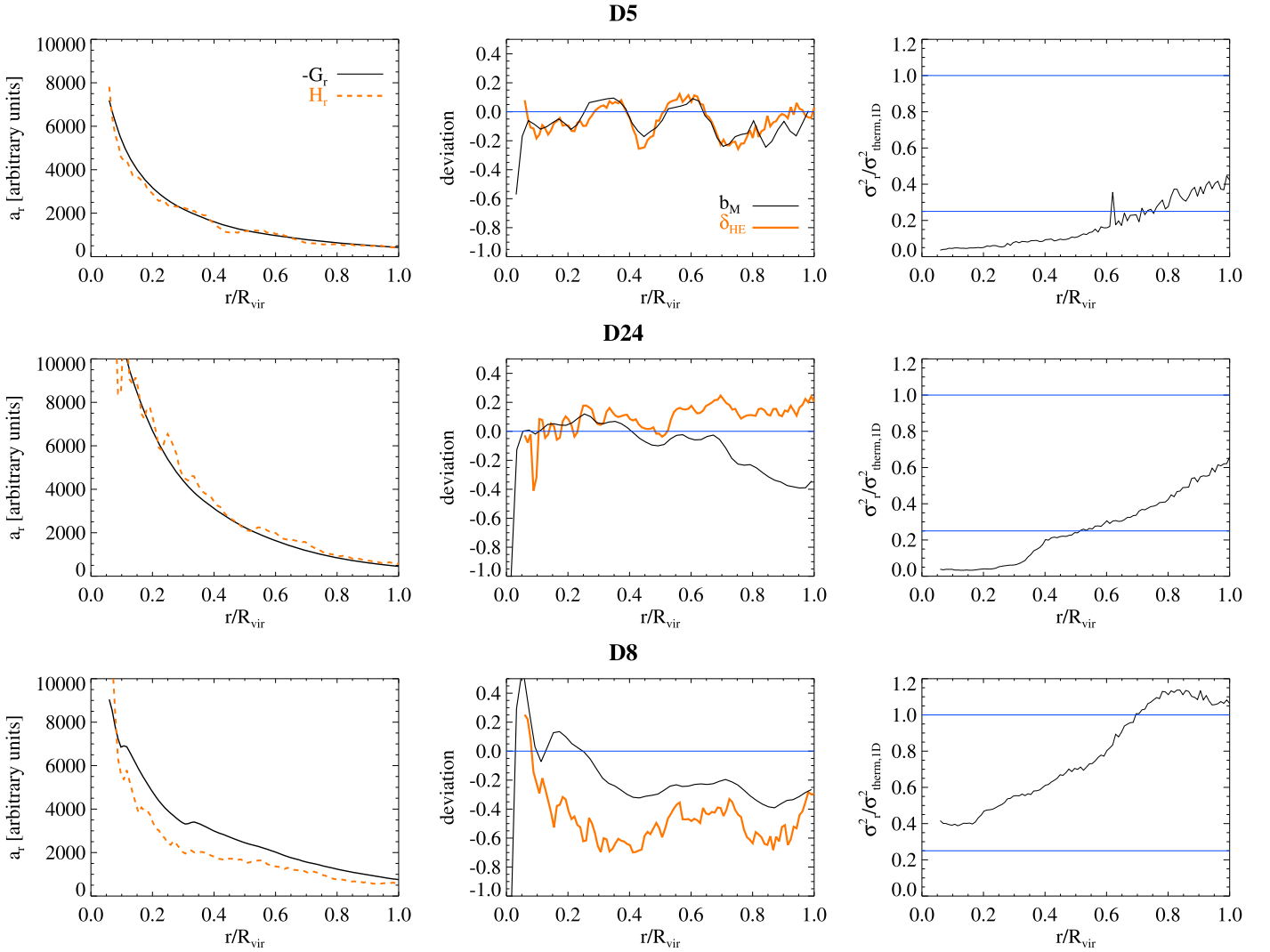


Figure 2. Three different clusters (D5, D24, and D8) in the sample chosen to represent two extreme cases and an intermediate one w.r.t., the comparison between the deviation from HE, traced by $\delta_{\text{HE}} = \mathcal{G}_r/\mathcal{H}_r + 1$, and mass bias b_M . From left to right, we show the radial profiles of the gravitational (\mathcal{G}_r , changed in sign; black solid line) and hydrodynamical (\mathcal{H}_r ; orange dashed line) accelerations (radial components); mass bias (b_M ; black line) and deviation from HE (δ_{HE} ; orange thick line); and the amount of non-thermal motions along the radial direction, with respect to thermal ones.

the velocity dispersion of the gas in the radial direction and $\sigma_{\text{therm,1D}}^2$ is the expected one-dimensional thermal velocity dispersion.¹² The thermal velocity dispersion is instead calculated as

$$\sigma_{\text{therm}}^2 = \frac{3k_B T_{\text{mw}}}{\mu m_p},$$

where T_{mw} is the mass-weighted temperature in the shell and for a single dimension $\sigma_{\text{therm,1D}}^2 = \sigma_{\text{therm}}^2/3$. in the same radial bin. The last quantity represents the excess of the velocity dispersion produced by bulk and random motions over the velocity dispersion produced by thermal motions.

The top- and bottom-row panels represent the opposite cases in which the profiles of b_M and δ_{HE} either trace each other in a very good way (as for D5) or show a significant offset (D8). In the first case, the mass bias more directly reflects the level of deviation from HE, suggesting that the additional assumption

of purely thermal pressure support—included in M_{HE} , but not involved in δ_{HE} —does not play a significant role. This is in fact supported by the low amount of non-thermal motions, with respect to thermal ones, shown in the right panel. Vice-versa, for D8, we notice a systematic difference between b_M and δ_{HE} , with the latter being much more significant than the mass bias, throughout the whole radial range. The origin of the significant deviation from HE on the radial direction is due to the systematic unbalance between the two forces, as is visible from the separate \mathcal{G}_r and \mathcal{H}_r profiles in the left panel. The mismatch between b_M and δ_{HE} is strongly connected to the behavior of the $\sigma_r^2/\sigma_{\text{therm,1D}}^2$ ratio, which significantly increases from 0.4 in the center¹³ out to more than one toward the virial radius, indicating that outside $\sim 0.7R_{\text{vir}}$ macroscopic non-thermal motions actually start to be dominant.

The halo presented in the middle row of Figure 2 (D24) represents instead an intermediate case where, despite the low-level deviation from $\mathcal{G}_r/\mathcal{H}_r = -1$ (δ_{HE} , mostly around 10% out

¹² Here, σ_r^2 is computed as the dispersion on the radial component of the gas velocities with respect to the mean value in each radial shell.

¹³ Here, and throughout the paper, the cluster center corresponds to the position of the DM particle having the minimum value of the potential.

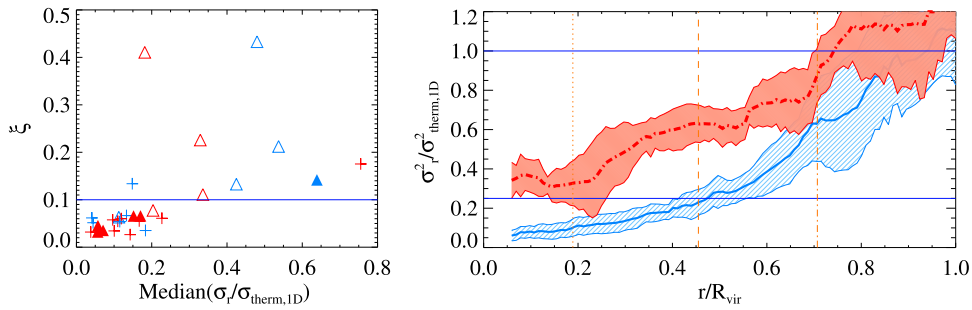


Figure 3. Left: relation of the median difference between the profiles of the mass bias and of the deviation from HE (quantified by ξ ; see Equation (6)), and the median value of the $\sigma_r^2/\sigma_{\text{therm,1D}}^2$ ratio, within R_{500} , for the 29 clusters in the sample. The horizontal line marks the threshold used to identify the subsample of clusters with large (small) differences between the b_M and δ_{HE} profiles, i.e., with $\xi > 0.1$ (< 0.1). The symbols and colors refer to the two classifications used to subdivide the sample, as specified in the following Section 4.4. Right: median radial profile of the $\sigma_r^2/\sigma_{\text{therm,1D}}^2$ ratio, distinguishing between two classes of clusters, i.e., those with $\xi < 0.1$ (blue solid line) and $\xi > 0.1$ (red dotted–dashed line), within R_{500} . Shaded areas mark the median absolute deviation in each radial bin. From left to right, vertical lines mark median values of R_{2500} , R_{500} , and R_{200} , respectively.

to the virial radius), the mass bias profile does show a different trend, especially toward the outer regions. The modulus of $\mathcal{G}_r/\mathcal{H}_r$ decreases with increasing radius, indicating that \mathcal{H}_r dominates over \mathcal{G}_r ,¹⁴ whereas the mass bias suggests the opposite unbalance between the hydrodynamical and the gravitational forces: $b_M < 0$, indeed, indicates that the thermal pressure support underestimates the gravitating mass.

The trend shown by the three examples in Figure 2 is in fact present in the entire sample, with large deviations from HE generally associated with substantial non-thermal motions of the gas. Furthermore, we notice that the profiles of \mathcal{G}_r and \mathcal{H}_r (left panels) indicate that the gravitational component is typically smoother than the hydrodynamical one and that halos with large deviations from HE also show a large offset of \mathcal{H}_r with respect to \mathcal{G}_r , with the latter generally dominating in modulus. In general, the origin of deviations from HE and its relation to the mass bias can significantly vary from cluster to cluster, requiring a dedicated investigation of the particular cluster properties. Nonetheless, from the analysis of all the 29 clusters, we can conclude that large differences between b_M and δ_{HE} typically correspond to $\sigma_r^2 \gtrsim 0.3 \sigma_{\text{therm,1D}}^2$, as observed, for example, in the extreme case of cluster D8, where $\sigma_r^2/\sigma_{\text{therm,1D}}^2$ is larger than 40% from the center out to the virial radius.

From a more quantitative perspective, we provide a measure of the typical difference between the two radial profiles of b_M and δ_{HE} as the median value of the absolute difference among the two, i.e.,

$$\xi = \text{Median}(|b_M - \delta_{\text{HE}}|), \quad (6)$$

considering the radial range up to R_{500} . The motivation to consider the region enclosed by R_{500} is that this is an optimal region targeted also by observational analyses, while outer portions of the cluster regions are generally more difficult to characterize. Furthermore, the amount of non-thermal motions in the radial direction generally increases toward the outskirts, where merging and accretion processes play a more significant role, for all the clusters. Also, the use of the median deviation allows us to estimate the typical difference between the two profiles, without being biased by large differences restricted to a few radial bins. As is visible from the left panel in Figure 3, it is possible to identify a subsample of clusters for which the

median difference between the b_M and δ_{HE} radial profiles, ξ , and the median value of $\sigma_r^2/\sigma_{\text{therm,1D}}^2$, are both very low within R_{500} . From this figure, we use the threshold $\xi = 0.1$ to separate these systems from those with larger values of both the indicators. The median radial profile of $\sigma_r^2/\sigma_{\text{therm,1D}}^2$ for these two subsamples of clusters is shown in the rhs panel of Figure 3, where the red, dotted–dashed curve represents the subsample, typically with different b_M and δ_{HE} profiles, while the blue, solid line indicates those with more similar ones ($\xi < 0.1$). The comparison of the two profiles confirms that larger differences between the b_M and δ_{HE} profiles (red curve) correspond to larger ($> 30\%$) amounts of non-thermal over thermal motions (in the radial direction), despite the larger dispersion¹⁵ in the subsample that only comprises 9 systems out of 29. We additionally note that the systematic offset visible out to R_{500} , which is in the region where the classification criteria are defined (Figure 3, left panel), is still present almost out to R_{200} ($\sim 0.7R_{\text{vir}}$). Both subsamples, instead, behave more similarly in the outermost region, where in fact the $\sigma_r^2/\sigma_{\text{therm,1D}}^2$ ratio increases for both classes.

As displayed by Figure 9 below, a similar behavior is recognized when the subsample is instead divided in regular and disturbed systems, with the second class typically showing a higher profile of the non-thermal to thermal motion ratio.

4.3. Average Deviation from HE

Overall, our results confirm that not only the hydrostatic mass bias, but also the level of deviation from the static assumption, δ_{HE} , is in fact very different from cluster to cluster and at different radii within the single object. This is consistent with the findings obtained in similar works based on AMR simulations (e.g., Lau et al. 2013; Nelson et al. 2014; Shi et al. 2015).

A possible way to investigate the problem is to consider samples of clusters and stack the individual profiles to infer an average behavior. In this way, the effects due to asphericity of

¹⁴ As is visible from the two acceleration profiles in the left panels, the sign of \mathcal{G}_r is negative, while the sign of \mathcal{H}_r is positive.

¹⁵ Here, and throughout the paper, we quantify the scatter around the median profile through the median absolute deviation, defined as

$$M. A. D. = \text{Median}(x_i - \text{Median}(x_i)),$$

with x_i representing the values of the individual profiles in every radial bin.

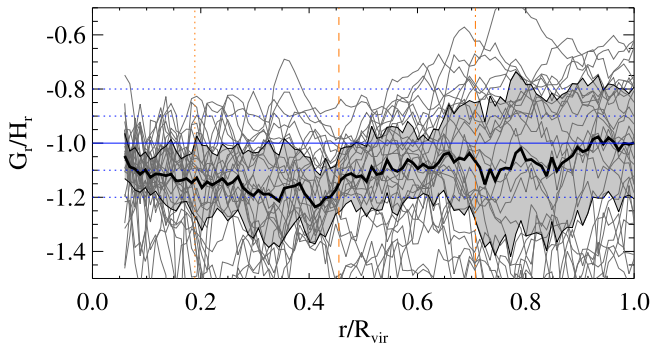


Figure 4. Median radial profile (black solid curve) of the ratio between the radial components of gravitational and hydrodynamical acceleration, for the main halos in the 29 resimulated regions. The light-gray lines in the background represent the individual G_r/H_r profiles of all the 29 halos. From left to right, vertical lines mark median values of R_{2500} , R_{500} , and R_{200} , respectively. We indicate with the shaded area the median absolute deviation from the the median profile.

the individual clusters are alleviated and the importance of the assumption of spherical symmetry is less significant.

The stack analysis is shown in Figure 4, where we display the individual profiles (gray curves) and the median one (black). The shaded area indicates the dispersion of the distribution in each radial bin around the median value, and is computed as the median absolute deviation. As is pointed out, the background individual profiles show very different features and the overall dispersion increases with the radius. In the outskirts, where the gas acceleration field is more sensitive to substructure infalling onto the main halo, the spread is larger. Nevertheless, the median profile indicates that the typical deviation of G_r/H_r from -1 is $\sim 10\%$, reaching $\sim 20\%$ at most.

Similarly, we can construct the median profile of the mass bias for the 29 halos in the sample, as shown in Figure 5. Without distinguishing the dynamical state of clusters, from the comparison between Figures 4 and 5, we see that the two median profiles of the acceleration term and the hydrostatic mass bias are quite similar out to $\sim 0.7 R_{\text{vir}}$ (roughly $\sim R_{200}$). This suggests that the negative mass bias does trace—on average—the violation of HE, i.e., the equilibrium is not static and the (total) acceleration term is non-zero.

The computation of the hydrostatic mass as in Equation (4) from X-ray data can include an additional bias due to the under-estimate of the X-ray temperature with respect to the dynamical temperature. A good approximation for the temperature measured by Chandra and XMM-Newton telescopes is provided by the so-called spectroscopic-like temperature T_{sl} (Mazzotta et al. 2004), which is commonly used in numerical simulations, and it is defined as

$$T_{\text{sl}} = \frac{\sum_i w_i T_i}{\sum_i w_i} \quad \text{with} \quad w_i = m_i \rho_i T_i^{-3/4}. \quad (7)$$

In Equation (7), m_i , ρ_i , T_i indicate the mass, density, and temperature of the single gas element in the simulation.¹⁶ It has been shown in previous works (e.g., Biffi et al. 2014) that due to the presence of inhomogeneities in the X-ray emitting gas there is a systematic difference between the spectroscopic-like estimate and the mass-weighted temperature (T_{mw}) that would

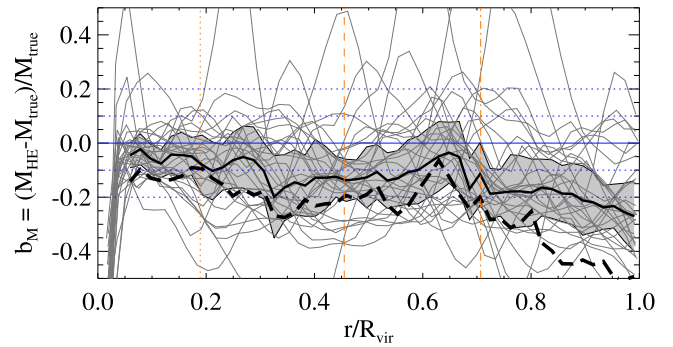


Figure 5. Median radial profile of the mass bias b_M , with M_{HE} calculated for both $T = T_{\text{mw}}$ (black solid line) and $T = T_{\text{sl}}$ (black dashed line). Only for the first case ($T = T_{\text{mw}}$), we also report the individual mass-bias profiles of the 29 clusters (light-gray curves) and the median absolute deviation from the median profile (shaded area). From left to right, vertical lines mark median values of R_{2500} , R_{500} , and R_{200} , respectively.

introduce an additional bias in M_{HE} (e.g., Rasia et al. 2014). The origin of such bias is, however, independent of the assumptions of HE or purely thermal pressure support, and only depends on the degree of thermal complexity of the ICM.

When the spectroscopic-like temperature T_{sl} is adopted, instead of T_{mw} , we observe the additional bias (black dashed curve in Figure 5) due to the different temperature estimation. In this case, the average bias ranges from $\sim 15\%$ to $\sim 25\%$ within R_{200} , while it is more significant in the cluster outer regions, increasing up to 50%.

Focusing on the outskirts, the trend of the average mass bias profile is different from the G_r/H_r one. Given the likely presence of infalling substructures, the hydrostatic estimate is, on average, significantly lower than the true mass, though the deviation from HE (quantified via G_r/H_r) is typically closer to zero. This suggests that, at such large radii, the origin of the mass bias is mostly related to the additional assumption of the purely thermal nature of the ICM pressure, involved in the computation of M_{HE} , rather than to a pure violation of the static state $dv/dt = 0$. Nevertheless, note that $G_r/H_r \sim -1$ only asserts the equilibrium in the radial direction, and differences in the anisotropy of the two acceleration components can also play a role, especially in the outskirts.

4.4. Distinguishing Among Cluster Populations

We proceed to evaluate the median mass bias and the δ_{HE} profiles for subsamples defined on the basis of either their thermal or dynamical processes. In particular, we consider here two classifications: (a) one linked to the cool-core-ness of the object and (b) the other to its global dynamical state. These two classifications are typical ways of distinguishing regular/disturbed clusters in observational (method a) and numerical (method b) studies.

Cool-core-ness. The classification (a) is based on the core thermal properties of the clusters, and specifically on the central entropy value. In more detail, we define the cluster as a cool-core (CC) if

$$\text{CC: } \begin{cases} K_0 < 60 \text{ keV cm}^{-2} \\ \sigma < 0.55 \end{cases} \quad (8)$$

and NCC otherwise (see Rasia et al. 2015 for more details on this classification). In Equation (8), K_0 is the central entropy derived from the fit of the cluster entropy profile and σ is the pseudo-

¹⁶ To calculate the spectroscopic-like temperature, all particles with temperatures below 0.3 keV have been discarded.

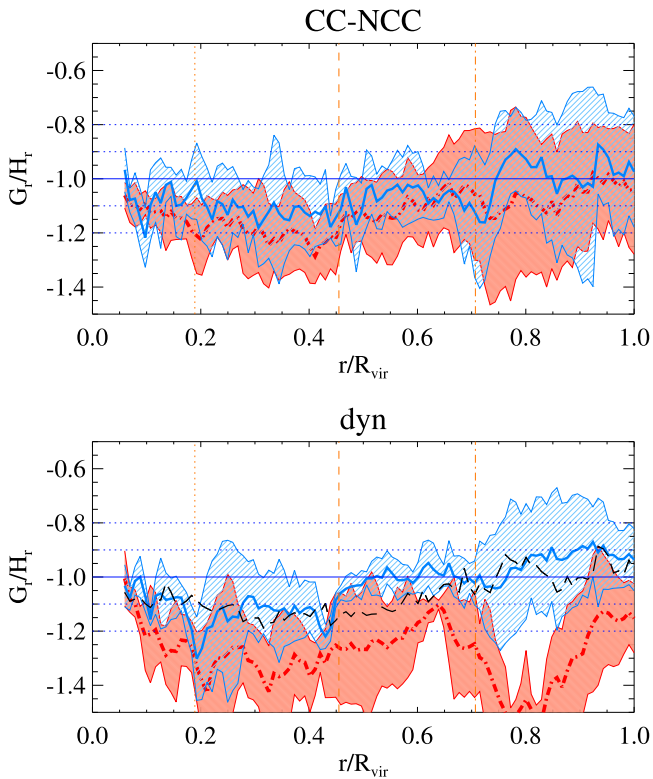


Figure 6. Median radial profile of $\mathcal{G}_r/\mathcal{H}_r$, as in Figure 4, distinguishing among different cluster populations. Shaded areas represent the median absolute deviation in each radial bin (w.r.t. the median value). Upper panel: CC/NCC (blue solid/red dotted–dashed line); lower panel: regular/disturbed (blue solid/red dotted–dashed line) clusters; intermediate systems are marked by the thin black line and, for simplicity, no dispersion is marked. From left to right, vertical lines mark median values of R_{2500} , R_{500} , and R_{200} , respectively.

entropy, defined as $\sigma = (T_{\text{IN}}/T_{\text{OUT}}) * (\text{EM}_{\text{IN}}/\text{EM}_{\text{OUT}})^{-1/3}$, with the temperature (T) and Emission Measure (EM) computed within the “IN” and “OUT” regions, corresponding to $R < 0.05 R_{180}$ and $0.05 R_{180} < R < 0.2 R_{180}$, respectively (see, e.g., Rossetti et al. 2011).

With this method, we classify 11 clusters out of 29 as CC, and the remaining 18 halos as NCC.

Dynamical state. The method (b), instead, combines two criteria commonly used in numerical simulations to classify a cluster as dynamically regular or disturbed: the center shift (δr), defined as the spatial separation between the position of the minimum of the potential and the center of mass, and the fraction of mass associated with substructures (f_{sub}). In our work, we define regular clusters as those for which

$$\left\{ \begin{array}{l} \delta r = \|\mathbf{x}_{\text{min}} - \mathbf{x}_{\text{cm}}\|/R_{200} < 0.07 \\ f_{\text{sub}} = \frac{M_{\text{tot, sub}}}{M_{\text{tot}}} < 0.1 \end{array} \right. , \quad (9)$$

where \mathbf{x}_{min} and \mathbf{x}_{cm} are, respectively, the position of the minimum of the potential and the center of mass, M_{tot} is the total mass and $M_{\text{tot, sub}}$ is the total mass in substructures. For values of δr and f_{sub} above those thresholds, the clusters are classified as disturbed. Similar conditions are adopted in Neto et al. (2007) and Meneghetti et al. (2014). Those systems for which the two criteria in (9) are not simultaneously satisfied are classified as intermediate systems. This second

classification defines the state of the cluster on more global scales, with the quantities above calculated for each cluster within R_{200} .

With this method we split the sample of 29 clusters into 6 regular and 8 disturbed systems and 15 intermediate cases.

4.4.1. The Ratio $\mathcal{G}_r/\mathcal{H}_r$

In the two panels of Figure 6, we show that the median profile of $\mathcal{G}_r/\mathcal{H}_r$ depends on the classification assumed.

When the sample is divided into CC and NCC clusters, as in the upper panel of Figure 6, there is no significant difference in the $\mathcal{G}_r/\mathcal{H}_r$ profile of the two populations, especially considering the dispersion around the median values. Overall, both behaviors are very similar to the median profile constructed from the whole sample (Figure 4).

A different picture emerges when the selection is made on the global dynamical properties. In this case (lower panel of Figure 6), the two populations show a clearer systematic offset, especially outside R_{2500} , with the largest departure in the region outside R_{200} ($\sim 0.7\text{--}0.9 R_{\text{vir}}$). We find that the median profile of regular clusters is systematically higher and closer to the HE value of -1 . On the contrary, disturbed clusters show a larger ($>20\%$) deviation from HE throughout the radial range.

We notice that this difference is not due to the presence of an intermediate class in the dynamical classification, which has no analogue in the CC-NCC one. In fact, by restricting the NCC subsample to the most extreme cases and thus introducing an intermediate class of objects, a similar separation to that observed between regular and disturbed clusters is still not found.

It is important to note that our sample of disturbed clusters are likely to be more strongly affected by merging events and accretion of infalling substructures, as confirmed also by their clumpiness profiles, presented by S. Planelles et al. (2016, in preparation). This should also reflect on a more significant difference in the (an)isotropy of the gravitational and hydrodynamical acceleration fields, likely to be enhanced at larger distances from the cluster center where the mass assembly is still ongoing.

In fact, we see from Figure 7 (bottom panel) that the gravitational acceleration is generally almost radial from the center out to the outskirts (typically $\mathcal{G}_r/|\mathbf{a}_g| \sim 0.9$), while the hydrodynamical acceleration shows a radial component that decreases with radius (from ~ 0.7 to ~ 0.5 , going from the center to R_{200}) and is almost isotropic in the intermediate region comprised between R_{500} and R_{200} . This is more evident for disturbed clusters, for which the profile of $\mathcal{H}_r/|\mathbf{a}_h|$ is systematically lower, namely less radial, than for regular systems. This offset is mirrored by the one in the $\mathcal{G}_r/\mathcal{H}_r$ profiles.

Instead, the same is not observed when the distinction between CC and NCC systems is adopted, as shown in the upper panel of Figure 7. In this case, the profiles of the two populations behave in a very similar way, for both the acceleration components.

4.4.2. Hydrostatic Mass Bias

Using the same selection criteria to investigate the mass bias, we obtain the results presented in Figure 8 (upper and lower panel, respectively). Here we only show the results for M_{HE} computed using the mass-weighted temperature. Although we verified that using the spectroscopic-like estimate, we obtain

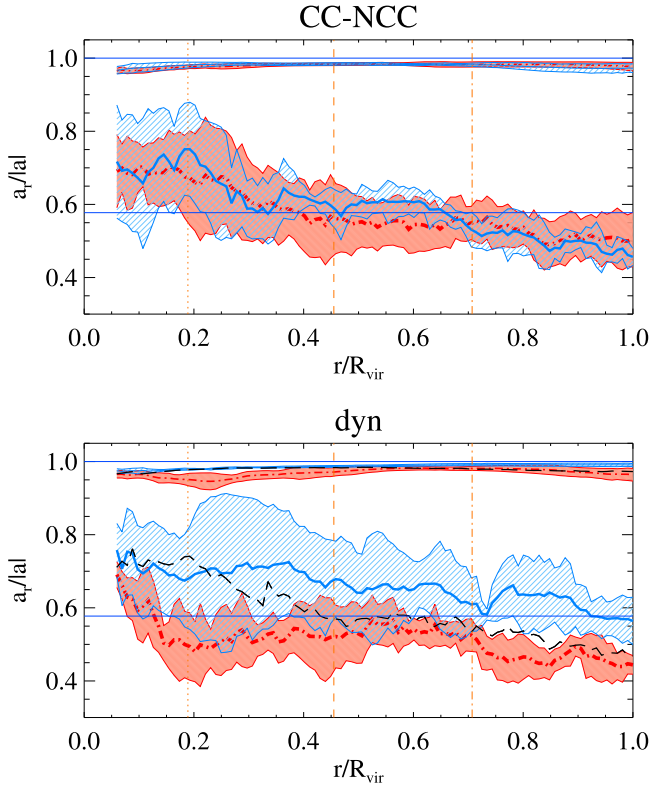


Figure 7. Median radial profile of the ratio between the radial component of the acceleration and the modulus of the total acceleration vector. This ratio quantifies the anisotropy of the—gravitational and hydrodynamical (thin and thick lines, respectively)—acceleration field: $a_r/|a| = 1 \rightarrow$ purely radial, $a_r/|a| = 1/\sqrt{3} \rightarrow$ isotropic (both marked by blue solid lines), and $a_r/|a| = 0 \rightarrow$ purely tangential. Shaded areas represent the median absolute deviation from the median value in each radial bin. Upper panel: CC/NCC (blue solid/red dotted–dashed line); lower panel: regular/disturbed (blue solid/red dotted–dashed line) clusters; intermediate systems are marked by the thin black line and, for simplicity, no dispersion is marked. From left to right, vertical lines mark median values of R_{2500} , R_{500} , and R_{200} , respectively.

very similar profiles, with the only difference being an overall more significant bias (as seen from Figure 5) and a larger scatter, especially outside R_{200} .

We note that the hydrostatic mass bias behaves differently from the acceleration term with respect to the classification adopted: no systematic distinction between regular and disturbed clusters is evident, except for the outermost region ($>0.7R_{\text{vir}}$). Instead, a separation, albeit relatively mild, is found between CC and NCC out to $\sim R_{2500}$, where there is an offset between their median profiles and the shaded areas marking the dispersion around the median values barely touch each other. In that inner region of the radial profile, the CC population presents almost zero mass bias, while the NCC subsample is characterized by a mass bias of roughly 10%–15%. This is mainly due to the different thermodynamical properties of the two classes in the innermost region, where CC clusters are typically characterized by a higher thermal pressure support with respect to NCC systems (see S. Planelles et al. 2016, in preparation), despite the similar shape of their potential well. This then results in a better match between the hydrostatic mass and the total gravitating mass.

Interestingly, the comparison between the lower panels of Figures 6 and 8 indicates that the hydrostatic mass bias of disturbed systems is on average $\lesssim 25\%$ (with peaks around 25%–30%) despite the larger deviation from -1 of $\mathcal{G}_r/\mathcal{H}_r$,

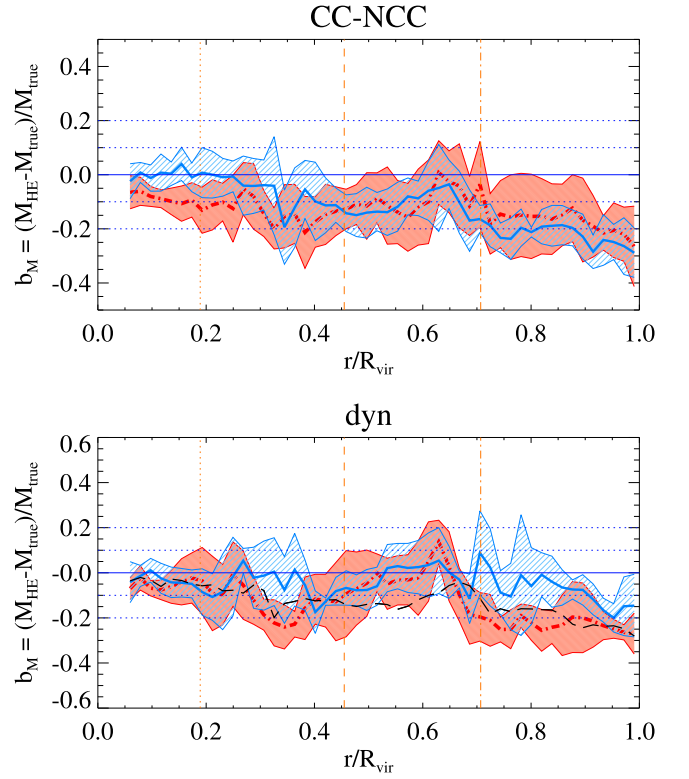


Figure 8. Median radial profile of the mass bias, as in Figure 5, distinguishing among different cluster populations. Upper panel: CC/NCC (blue solid/red dotted–dashed line); lower panel: regular/disturbed (blue solid/red dotted–dashed line) clusters; intermediate systems are marked by the thin black line and, for simplicity, no dispersion is marked. The hydrostatic mass, M_{HE} , is calculated using T_{mw} . Shaded areas represent the median absolute deviation from the median value, in each radial bin. From left to right, vertical lines mark median values of R_{2500} , R_{500} , and R_{200} , respectively.

(mostly $\delta_{\text{HE}} > 20\%$, up to 50%). The origin of a deviation from zero acceleration (on the radial direction) that is larger than the violation of the balance between gravitational and thermal pressure forces, must be related to gas non-thermalized motions, that are not accounted for in our computation of ∇P (where $P = P_{\text{th}} \propto \rho T$).

From Figures 6 and 7 (and Figure 9 below), we conclude that the radial properties of the ICM acceleration field, and thus the level of HE, are not very sensitive to the cool-core-ness of the system, but rather depend on its global dynamical state, whereas the mass bias is more closely related to the cool-core-ness, and so to thermal properties, especially in the central regions (see Figure 8).

Differences between the $\mathcal{G}_r/\mathcal{H}_r$ and mass bias radial profiles can also be related to the presence of non-thermal, bulk and random, motions in the gas, as discussed in Section 4.2. Here, we present median stacked profiles of $\sigma_r^2/\sigma_{\text{therm,1D}}^2$ for the subsamples defined on the basis of the cluster cool-core-ness or dynamical classification, in analogy to Figures 6 and 8. From Figure 9, we infer that CC and NCC (upper panel) behave in a very similar way, with a similar amount of non-thermal motions increasing toward larger distances from the center. On the contrary, disturbed systems clearly differentiate from dynamically regular ones (lower panel) for the presence of a more substantial amount of radial non-thermal motions with respect to thermal ones already in the innermost region and out to the virial radius (systematically higher values of

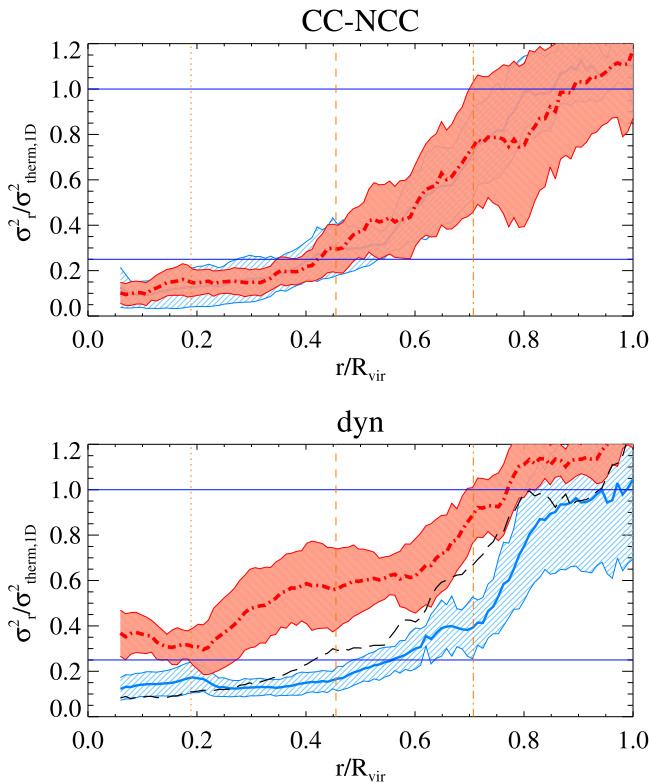


Figure 9. Median radial profile of $\sigma_r^2/\sigma_{\text{therm,1D}}^2$, distinguishing among different cluster populations. Upper panel: CC/NCC (blue solid/red dotted–dashed line); lower panel: regular/disturbed (blue solid/red dotted–dashed line) clusters; intermediate systems are marked by the thin black line and, for simplicity, no dispersion is marked. Shaded areas represent the median absolute deviation from the median value in each radial bin. From left to right, vertical lines mark median values of R_{2500} , R_{500} , and R_{200} , respectively.

$\sigma_r^2/\sigma_{\text{therm,1D}}^2$). So the conclusion is that mass bias and HE-violations are two different things, the first more related to cool-core-ness, the second more related to the dynamical state of the cluster.

In addition to their radial dependence, it is useful to evaluate the relation between mass bias and deviation from HE at interesting distances from the cluster center, such as R_{2500} , R_{500} , and R_{200} (see Figure 10). Despite a larger scatter in the outskirts, the two quantities closely trace each other, as indicated by the Pearson correlation coefficient for the three relations: 0.73, 0.72, 0.69, for R_{2500} , R_{500} , and R_{200} , respectively. The significance of this result is confirmed by corresponding p -values of the correlation coefficients of 8.1×10^{-6} , 1.1×10^{-5} , and 3.3×10^{-5} . In particular, this result is stronger for the subsample of regular systems, for which the correlation coefficients range from 0.88 at R_{2500} to 0.86 at R_{200} (with p -values of order of 0.02–0.03). Then, mass bias and violation of HE are correlated with each other despite reflecting different aspects of clusters. The outliers of this correlation tend to be disturbed clusters and typically reside in the upper envelope of the relation (higher b_M and lower δ_{HE} than expected from the linear correlation).

In Table 1, we report the median values, with 1σ errors, of the b_M and δ_{HE} distributions shown in Figure 10. We note that these results correspond to single radial bins (at R_{2500} , R_{500} , and R_{200} , respectively) in the profiles discussed in the previous sections.

4.5. Correlation with Temperature Bias

For the purpose of our investigation, it is important to explore the thermal structure of the ICM and the presence of temperature inhomogeneities, which might affect both the level of HE and the bias on the hydrostatic mass derived.

Numerically, this can be evaluated by comparing the mass-weighted and spectroscopic-like estimates of temperature, T_{mw} and T_{sl} , where the former is a more dynamical measurement and the latter is more sensitive to the multi-phase nature of the gas.

One common way of evaluating this is to calculate the so-called temperature bias, defined as

$$b_T = (T_{\text{sl}} - T_{\text{mw}})/T_{\text{mw}}. \quad (10)$$

In Figure 11, we report the radial profile of the temperature bias for the 29 halos (left panel, top) for which we also show the median profiles for the CC and NCC populations, separately (left panel, bottom). On average, b_T is always negative out to the virial radius, indicating that, locally, the spectroscopic-like temperature typically underestimates the dynamical measurement (T_{mw}), at all distances from the cluster center. Nevertheless, the average bias is found to be quite small, indicating a relatively homogeneous temperature structure for both categories, out to $\sim R_{500}$ (i.e., $\sim 0.4R_{\text{vir}}$), with $b_T \lesssim 10\%$. This can be explained by the improved gas mixing that characterizes these new simulation runs, which allows the gas stripped from the substructures to efficiently mix and better thermalize with the surrounding ambient ICM. In the innermost cluster region the difference between CC and NCC temperature profiles, decreasing in the first case and flattening or even rising in the other, is not caught by the temperature bias profile. The reason for this is that the region sampled by each central radial bin is not extended enough to capture the central temperature gradient typical of CC. In the outer part of the profile, enclosed between R_{500} and R_{200} , the bias remains relatively low for CC systems, whereas the mismatch between T_{sl} and T_{mw} increases for NCC. Toward the virial radius, the bias significantly increases for both classes.

In the right panel of Figure 11, we report the direct comparison of the global estimates of T_{mw} and T_{sl} , for the region enclosed by R_{500} , by showing the temperature bias as a function, e.g., of T_{mw} . Considering the large variety of dynamical states among the clusters in the sample, we observe, on average, a very good agreement between the two values, with T_{sl} typically underestimating T_{mw} by only a few percent (within R_{500} , the median value of the bias is ~ 5). From this relation, we also note that there is no evidence for a dependence of the temperature bias on the global dynamical temperature of the systems. In fact, given the well-defined relation between temperature and mass for the clusters analyzed (see Truong et al., in preparation), we also verified that there is no clear dependence of the temperature bias on the total cluster mass.

HE is however a local condition and ultimately depends on the local thermodynamical properties of the ICM. Thus, it is interesting to evaluate the relation between deviation from HE, mass bias, and temperature bias, as in Figure 12, via the dependence of b_M and δ_{HE} (in the upper and lower panels, respectively) on the b_T , at interesting distances from the cluster center, i.e., R_{2500} , R_{500} , and R_{200} .

Marking the clusters with different symbols and colors, depending on their cool-core-ness or dynamical classification,

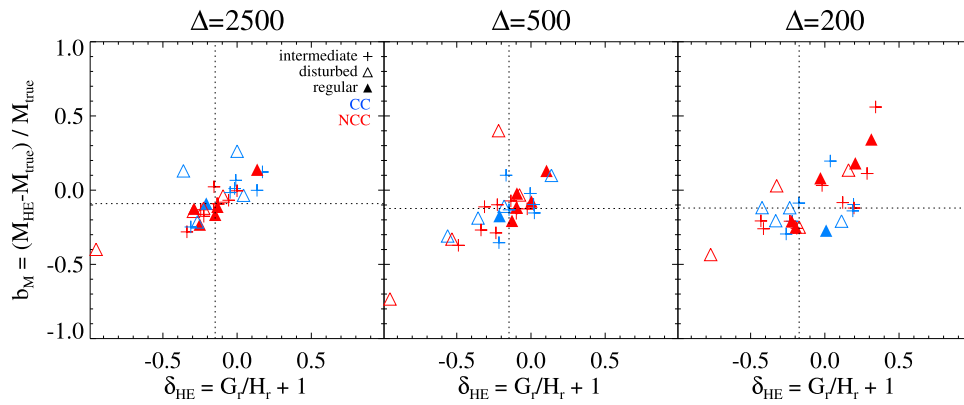


Figure 10. Relation between mass bias (b_M) and deviation from HE (δ_{HE}), calculated at R_{2500} (left), R_{500} (middle), and R_{200} (right). In each panel, median values of the distributions are indicated by the dotted lines.

Table 1

Median Values and Errors of the Mass Bias (Top, b_M) and Deviation from HE (Bottom, δ_{HE}) Reported in Figure 10, Calculated at R_{2500} , R_{500} , and R_{200} for the Various Subsamples Considered

	$\Delta = 2500$	$\Delta = 500$	$\Delta = 200$
b_M			
All	-0.091 ± 0.016	-0.123 ± 0.015	-0.120 ± 0.024
CC	-0.001 ± 0.027	-0.132 ± 0.017	-0.140 ± 0.020
NCC	-0.123 ± 0.011	-0.119 ± 0.021	-0.102 ± 0.036
Regular	-0.118 ± 0.015	-0.095 ± 0.031	-0.065 ± 0.080
Disturbed	-0.080 ± 0.035	-0.148 ± 0.060	-0.162 ± 0.024
δ_{HE}			
All	-0.148 ± 0.022	-0.148 ± 0.016	-0.173 ± 0.039
CC	-0.017 ± 0.046	-0.168 ± 0.049	-0.175 ± 0.055
NCC	-0.157 ± 0.019	-0.132 ± 0.024	-0.101 ± 0.057
Regular	-0.178 ± 0.024	-0.096 ± 0.027	-0.010 ± 0.081
Disturbed	-0.247 ± 0.047	-0.287 ± 0.080	-0.281 ± 0.044

we mainly note a difference between regular and disturbed systems (filled and empty symbols in the figure), especially in terms of scatter, which is significantly larger for the disturbed ones. This is particularly evident for the values corresponding to R_{500} and R_{200} , where there is a more clear separation between the two dynamical classes, especially in terms of temperature bias.

Overall, we conclude from Figure 12 that the local level of HE and mass bias are not significantly affected by the local inhomogeneities in the ICM temperature structure. This is quantified by very low values of the Pearson correlation coefficients of the b_M - b_T and δ_{HE} - b_T relations, which only reach a maximum of ~ 0.3 for R_{500} and is very poorly constrained (p -values > 0.1). Only the CC subsample shows evidence of a significant correlation between δ_{HE} and temperature bias, especially in the outskirts—with a Pearson correlation coefficient (p -value) of $\sim 0.68(0.02)$ at R_{500} and $\sim 0.66(0.03)$ at R_{200} .

5. DISCUSSION AND CONCLUSION

The violation of HE in galaxy clusters has been widely studied from the numerical point of view in order to trace its origin and its connection to the bias in the mass reconstruction based on the HE hypothesis.

Here, we explored the violation of HE in the ICM by studying the balance between gravitational and hydrodynamical acceleration in the radial direction. This allowed us to investigate the level of deviation from HE per se, i.e., separately from the mass bias, which additionally implies the assumption of purely thermal pressure support (with $P_{\text{th}} \propto \rho T$).

In the following, we summarize our main findings.

1. Corrections for HE-violation based on the acceleration term for individual clusters are not really achievable. The differences from case to case, and depending on the distance from the cluster center, make the prediction of a single correction term very challenging, even by means of numerical simulations. This is noticeable from the significant scatter in the radial profiles of $\mathcal{G}_r/\mathcal{H}_r$.
 2. The classification of relaxed and un-relaxed clusters can be misleading, especially when simulations and observations are compared: depending on which cluster properties are used to define the level of regularity, the differences among the populations range from substantial to negligible. Caution is necessary when numerical results, e.g., scaling relations, are compared to observed ones, and vice versa.
 3. The acceleration term, quantified via the $\mathcal{G}_r/\mathcal{H}_r$ ratio, shows a systematic difference between the median radial profile of dynamically regular clusters and that of disturbed ones, with the latter showing a larger deviation from HE ($\delta_{\text{HE}} > 20\%$), i.e., from $dv/dt = 0$ (on the radial direction). This is especially significant in the outskirts ($\delta_{\text{HE}} \sim 50\%$).
- Instead, we find no clear dependence of the $\mathcal{G}_r/\mathcal{H}_r$ profile on the system cool-core-ness, from comparing CC and NCC median profiles.
4. On the contrary, when the hydrostatic mass bias is concerned, CC and NCC clusters behave differently, especially in the inner region ($\lesssim R_{2500}$), whereas no significant distinction is observed between the mass bias of regular and disturbed clusters, given the large dispersion.
 5. Typically, we find that the clusters for which the radial profile of mass bias and deviation from HE (δ_{HE}) poorly trace each other present a significant amount of non-thermal (bulk and random) gas motions with respect to thermal ones, in the radial direction, quantified by $\sigma_r^2/\sigma_{\text{therm,1D}}^2 > 0.3$ already in the innermost regions.

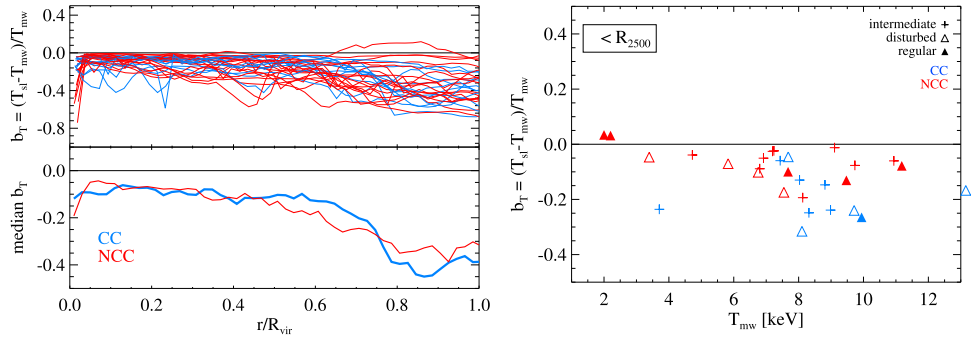


Figure 11. Left: radial profile of the temperature bias $b_T = (T_{sl} - T_{mw})/T_{mw}$, for the 29 main halos of this work (top panel). In the bottom panel, the median profiles for CC and NCC are shown. Colors refer to CC (blue) and NCC (red) clusters, as in the legend. Right: temperature bias as a function of T_{mw} , for the average temperatures within R_{500} , for the 29 halos; color code marks the CC/NCC (blue/red) classification while symbols distinguish among regular, disturbed, and intermediate systems.

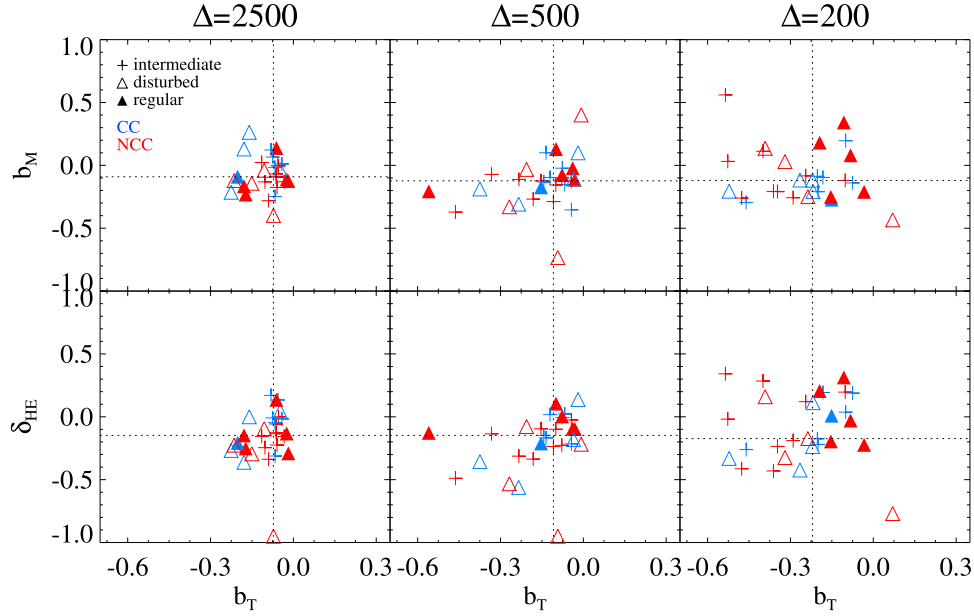


Figure 12. Dependence of mass bias (b_M ; upper panels) and deviation from HE (δ_{HE} ; lower panels) on the temperature bias (b_T), calculated at R_{2500} (left), R_{500} (middle), and R_{200} (right). In each panel, median values of the distributions are indicated by the dotted lines.

6. We also find a clear correlation between values of the hydrostatic mass bias and the deviation from HE computed at R_{2500} , R_{500} , and R_{200} , with the main outliers in this picture represented by dynamically disturbed systems. From this, we conclude that the local deviation from HE is of the order of 15%–20% (increasing toward the outskirts), and it is generally well traced by the local mass bias (of the order of 10%–15%).
7. The temperature structure of the clusters in the sample appears to be relatively regular, with a temperature bias lower than what was previously found in SPH simulations. In fact, we find that T_{sl} typically underestimates T_{mw} by a few percent in the innermost region, increasing up to $\sim 15\%$ – 20% toward the outskirts.
8. On average, we find no strong correlation between the local dishomogeneity in the thermal structure (quantified by the temperature bias) and the local deviation from HE or mass bias.

Simulations are extremely powerful for in-depth studies like the one presented in our analysis, since the HE validity in the

ICM of clusters can be explored in full detail cluster-by-cluster. In particular, we have shown different levels of deviation from HE and of hydrostatic mass bias for various cluster populations, classified on the basis of their global dynamical state—as often done in simulations—and core thermal properties—as typically done in observations. This was possible by employing state-of-the-art cosmological simulations that include the description of several hydrodynamical processes taking place in galaxy clusters and, most importantly, that were able to generate the observed coexistence of CC and NCC systems with thermo and chemodynamical properties in good agreement with observations (Rasia et al. 2015). We have shown that CC and dynamically regular clusters are very different populations in terms of HE-deviation and mass bias, and similarly NCC clusters clearly differ from disturbed systems in the same respect.

Nevertheless, such numerical studies also represent the intrinsic difficulty of predicting from simulations an accurate correction to X-ray based (or more in general to hydrostatic) masses on a cluster-by-cluster basis. Still, the virtue of simulations is that they allow us to calibrate such a correction

in a statistical sense, through the calibration of scaling relations between true masses and hydrostatic masses. Clearly, the reliability of these corrections, in view of their application to precision cosmology with clusters, depends on the degree of realism of the simulations. In this respect, additional forces, not treated in our work, should also be taken into consideration in cluster simulations, such as magnetic field and cosmic ray pressure, which alter the momentum of the intracluster gas in real clusters and can contribute to the support against the gravitational force.

From the observational point of view, up-coming (ASTRO-H) and future (e.g., Athena) X-ray missions, thanks to their high-resolution spectrometry capabilities, will help to better characterize the various terms of pressure support against gravity in clusters. This will be achieved via measurements of the gas velocities from non-thermal broadening and center shifts of spectral emission lines from heavy ions, e.g., iron. Even though the chance to measure gas accelerations still remains remote, if not impossible, future X-ray observations will likely permit us to reduce and control the effect due to the assumption of HE and to obtain more accurate mass estimates, especially from spatially resolved observations.

Additionally, given the distinct level of deviation from HE depending on the cluster dynamical state, rather than on their cool-core-ness, the possibility to observationally constrain the amount of non-thermal motions in the ICM could provide a new, complementary way of classifying cluster populations.

We are greatly indebted to Volker Springel for giving us access to the developer version of the GADGET3 code. We acknowledge financial support from PIFI-GA- 2013-627474, NSF AST-1210973, PRIN-MIUR 201278X4FL, PRIN-INAF 2012 “The Universe in a Box: Multi-scale Simulations of Cosmic Structures,” the INFN INDARK grant, “Consorzio per la Fisica” of Trieste, CONICET, and FONCYT, Argentina. Simulations were carried out using the Flux HCP Cluster at the University of Michigan, Galileo at CINECA (Italy), with CPU time assigned through ISCR proposals and an agreement with the University of Trieste, and PICO at CINECA through our expression of interest. S.P. acknowledges support by the Spanish Ministerio de Economía y Competitividad (MINECO, grants AYA2013-48226-C3-2-P) and the Generalitat Valenciana (grant GVACOMP2015-227). M.G. is supported by NASA through Einstein Postdoctoral Fellowship Award Number PF-160137 issued by the Chandra X-ray Observatory Center, which is operated by the SAO for and on behalf of NASA under contract NAS8-03060. A.M.B. is supported by the DFG Research Unit 1254 “Magnetisation of interstellar and intergalactic media” and by the DFG Cluster of Excellence “Universe.” Also, we would like to thank the anonymous referee for a careful reading of the manuscript and constructive comments that helped improve the presentation of this work.

APPENDIX THE HYDROSTATIC SPHERE TEST

In order to test the approach used in this work, we set up a sphere in HE as a study case and apply the analysis of the acceleration components presented above.

The hydrostatic sphere is set up with a total virial mass of $4 \times 10^{14} h^{-1} M_{\odot}$, resolved with 369300 DM particles and 403508 gas particles. The mass resolution is

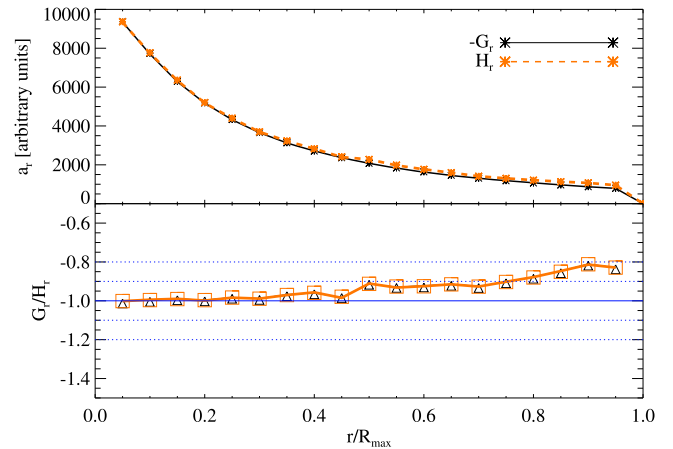


Figure 13. Hydrostatic sphere. Top panel: radial profiles of the \mathcal{G}_r (changed in sign, for visualization and comparison purposes) and \mathcal{H}_r components, as in the legend. Bottom panel: radial profile of the (mean and median) $\mathcal{G}_r/\mathcal{H}_r$ profile, both from the particle-based calculation (black triangles and solid line) and from the two separate components profiles (orange squares and dotted-dashed line). In both panels, symbols and lines indicate mean and median values, respectively.

$m_{\text{DM}} = 3.1 \times 10^9 M_{\odot}$ and $m_{\text{gas}} = 6.2 \times 10^8 M_{\odot}$, for DM and gas respectively. The simulation of the hydrostatic sphere has been performed with the same version of the code used for the other halos analyzed in this work, but including only non-radiative hydrodynamics. It has been evolved for a large enough number of dynamical time-steps until an ideal configuration of HE is reached.

As is visible from the \mathcal{G}_r (changed in sign) and \mathcal{H}_r profiles in Figure 13 (upper panel), the HE configuration shows very good balance between the two components out to very large radii, with their ratio showing almost perfect balance in the central region ($\delta_{\text{HE}} \lesssim 5\%$), and presenting deviations from HE smaller than 10% roughly out to R_{200} (~ 1200 kpc, i.e., $0.8 R_{\text{max}}$ in the figure). In fact, from the inspection of the $\mathcal{G}_r/\mathcal{H}_r$ profile at different time-steps, until the final configuration shown in Figure 13 (lower panel), we observe a clear trend of the profile to set toward the -1 reference line, with the radial range in which the equilibrium condition is satisfied extending outward. Given this, we expect that a perfect HE profile would be reached after an ideally large number of dynamical times. From the comparison with the various profiles obtained for the cosmological cases, presented in the previous sections, we estimate this effect not to cause any bias to the conclusions drawn from our study.

This study case is used to confirm that the HE, on the radial direction, corresponds indeed to $\mathcal{G}_r/\mathcal{H}_r \sim -1$, i.e., to the balance of the radial components of gravitational and hydrodynamical accelerations.

From the comparison in the figure between the profiles of \mathcal{G}_r , \mathcal{H}_r , and $\mathcal{G}_r/\mathcal{H}_r$, we additionally tested that

- i. the particle-based approach and the use of the separate profiles of \mathcal{G}_r and \mathcal{H}_r converge to the same result for an ideal hydrostatic gas distribution (perfect overlap between symbols (mean values) and lines (median values) in the lower panel); and
- ii. mean and median values within the radial bins provide exactly the same result (perfect overlap between curves and symbols), given the absence of gas inhomogeneities.

REFERENCES

- Applegate, D. E., Mantz, A., Allen, S. W., et al. 2015, *MNRAS*, 457, 1522
- Beck, A. M., Murante, G., Arth, A., et al. 2016, *MNRAS*, 455, 2110
- Biffi, V., Dolag, K., & Böhringer, H. 2011, *MNRAS*, 413, 573
- Biffi, V., Dolag, K., & Böhringer, H. 2013, *MNRAS*, 428, 1395
- Biffi, V., Sembolini, F., De Petris, M., et al. 2014, *MNRAS*, 439, 588
- Bonafede, A., Dolag, K., Staszczyn, F., Murante, G., & Borgani, S. 2011, *MNRAS*, 418, 2234
- Donahue, M., Voit, G. M., Mahdavi, A., et al. 2014, *ApJ*, 794, 136
- Ettori, S., Pratt, G. W., de Plaa, J., et al. 2013, arXiv:1306.2322
- Fang, T., Humphrey, P., & Buote, D. 2009, *ApJ*, 691, 1648
- Gaspari, M., Brighenti, F., & Temi, P. 2015, *A&A*, 579, A62
- Gaspari, M., & Churazov, E. 2013, *A&A*, 559, A78
- Gaspari, M., Churazov, E., Nagai, D., Lau, E. T., & Zhuravleva, I. 2014, *A&A*, 569, A67
- Jeltema, T. E., Hallman, E. J., Burns, J. O., & Motl, P. M. 2008, *ApJ*, 681, 167
- Kravtsov, A. V., & Borgani, S. 2012, *ARA&A*, 50, 353
- Lau, E. T., Kravtsov, A. V., & Nagai, D. 2009, *ApJ*, 705, 1129
- Lau, E. T., Nagai, D., & Nelson, K. 2013, *ApJ*, 777, 151
- Mahdavi, A., Hoekstra, H., Babul, A., et al. 2013, *ApJ*, 767, 116
- Mahdavi, A., Hoekstra, H., Babul, A., & Henry, J. P. 2008, *MNRAS*, 384, 1567
- Mazzotta, P., Rasia, E., Moscardini, L., & Tormen, G. 2004, *MNRAS*, 354, 10
- Meneghetti, M., Rasia, E., Merten, J., et al. 2010, *A&A*, 514, A93
- Meneghetti, M., Rasia, E., Vega, J., et al. 2014, *ApJ*, 797, 34
- Nandra, K., Barret, D., Barcons, X., et al. 2013, arXiv:1306.2307
- Nelson, K., Lau, E. T., Nagai, D., Rudd, D. H., & Yu, L. 2014, *ApJ*, 782, 107
- Nelson, K., Rudd, D. H., Shaw, L., & Nagai, D. 2012, *ApJ*, 751, 121
- Neto, A. F., Gao, L., Bett, P., et al. 2007, *MNRAS*, 381, 1450
- Nevalainen, J., David, L., & Guainazzi, M. 2010, *A&A*, 523, 22
- Pellegrini, S., & Ciotti, L. 2006, *MNRAS*, 370, 1797
- Piffaretti, R., & Valdarnini, R. 2008, *A&A*, 491, 71
- Planelles, S., Borgani, S., Fabjan, D., et al. 2014, *MNRAS*, 438, 195
- Rasia, E., Borgani, S., Murante, G., et al. 2015, *ApJL*, 813, L17
- Rasia, E., Ettori, S., Moscardini, L., et al. 2006, *MNRAS*, 369, 2013
- Rasia, E., Lau, E. T., Borgani, S., et al. 2014, *ApJ*, 791, 96
- Rasia, E., Tormen, G., & Moscardini, L. 2004, *MNRAS*, 351, 237
- Rossetti, M., Eckert, D., Cavalleri, B. M., et al. 2011, *A&A*, 532, A123
- Schellenberger, G., Reiprich, T. H., Lovisari, L., Nevalainen, J., & David, L. 2015, *A&A*, 575, 30
- Sereni, M., & Ettori, S. 2015, *MNRAS*, 450, 3633
- Shi, X., Komatsu, E., Nagai, D., & Lau, E. T. 2015, *MNRAS*, 455, 2936
- Simet, M., Battaglia, N., Mandelbaum, R., & Seljak, U. 2015, arXiv:1502.01024
- Smith, G. P., Mazzotta, P., Okabe, N., et al. 2016, *MNRAS*, 456, L74
- Springel, V. 2005, *MNRAS*, 364, 1105
- Springel, V., & Hernquist, L. 2003, *MNRAS*, 339, 289
- Steinborn, L. K., Dolag, K., Hirschmann, M., Prieto, M. A., & Remus, R.-S. 2015, *MNRAS*, 448, 1504
- Suto, D., Kawahara, H., Kitayama, T., et al. 2013, *ApJ*, 767, 79
- Tornatore, L., Borgani, S., Dolag, K., & Matteucci, F. 2007, *MNRAS*, 382, 1050
- Tornatore, L., Borgani, S., Matteucci, F., Recchi, S., & Tozzi, P. 2004, *MNRAS*, 349, L19
- Vazza, F., Brunetti, G., Kritsuk, A., et al. 2009, *A&A*, 504, 33
- von der Linden, A., Mantz, A., Allen, S. W., et al. 2014, *MNRAS*, 443, 1973